AGU PUBLICATIONS

JGR

Journal of Geophysical Research: Atmospheres

RESEARCH ARTICLE
10.1002/2017JD026833

Key Points:
- New, high-sensitivity two-filter radon detector was installed in Terra Nova Bay
- A technique was developed to distinguish between tropospheric subsidence and synoptic MBL events for coastal Antarctica
- Average coastal radon source function constrained for Terra Nova Bay region

Correspondence to:
S.-B. Hong,
hong909@kopri.re.kr

Citation:
Chambers, S. D., Choi, T., Park, S.-J., Williams, A. G., Hong, S.-B., Tositti, L., … Pereira, E. (2017). Investigating local and remote terrestrial influence on air masses at contrasting Antarctic sites using Radon-222 and back trajectories. *Journal of Geophysical Research: Atmospheres*, *122*. https://doi.org/10.1002/2017JD026833

Received 23 MAR 2017
Accepted 26 NOV 2017
Accepted article online 2 DEC 2017

Investigating Local and Remote Terrestrial Influence on Air Masses at Contrasting Antarctic Sites Using Radon-222 and Back Trajectories

S. D. Chambers[1], T. Choi[2], S.-J. Park[2], A. G. Williams[1], S.-B. Hong[2], L. Tositti[3], A. D. Griffiths[1], J. Crawford[1], and E. Pereira[4]

[1]Australian Nuclear Science and Technology Organisation, Kirrawee DC, New South Wales, Australia, [2]Korea Polar Research Institute, Incheon, South Korea, [3]Laboratorio di Radiochimica Ambientale, Dipartimento di Chimica "G.Ciamician", Università di Bologna, Bologna, Italy, [4]Instituto Nacional de Pesquisas Espaciais, S. José dos Campos, Brazil

Abstract We report on the first summer of high-sensitivity radon measurements from a two-filter detector at Jang Bogo Station (Terra Nova Bay) and contrast them with simultaneous observations at King Sejong Station (King George Island). King Sejong radon concentrations were characteristic of a marine baseline station (0.02–0.3 Bq m^{-3}), whereas Jang Bogo values were highly variable (0.06–5.2 Bq m^{-3}), mainly due to emissions from exposed coastal ground (estimated mean flux 0.09–0.11 atoms cm^{-2} s^{-1}) and shallow atmospheric mixing depths. For wind speeds of ≤3.5 m s^{-1} the influence of local radon emissions became increasingly more prominent at both sites. A cluster analysis of back trajectories from King Sejong (62°S) revealed a fairly even distribution between air masses that had passed recently over South America, the Southern Ocean, and Antarctica, whereas at Jang Bogo (75°S) 80% of events had recently passed over the Ross Ice Shelf and West Antarctica, 12% were synoptically forced over Cape Adare, and 8% were associated with subsidence over the Antarctic interior and katabatic flow to the station. When cross-checked against radon concentrations, only half of the back trajectories ending at Jang Bogo that had indicated distant contact with nonpolar southern hemisphere continents within the past 10 days showed actual signs of terrestrial influence. A simple-to-implement technique based on high-pass filtered absolute humidity is developed to distinguish between predominantly katabatic, oceanic, and near-coastal air masses for characterization of trace gas and aerosol measurements at coastal East Antarctic sites.

1. Introduction

Antarctica is remote, largely sheltered from the direct influence of other continents by the Southern Ocean, polar front, and polar vortex. Its relative isolation provides an ideal location to investigate long-term trends in atmospheric trace constituents. Antarctica also offers near-pristine conditions under which to study a variety of natural chemical processes (Davis et al., 2001; Grannas et al., 2007; Weller et al., 2002), some rather exotic by virtue of the extreme temperature and radiation conditions under which they occur. Particulate impurities in snow and ice cores, however, provide evidence of occasional atmospheric transport from lower latitude continental regions (e.g., Barbante et al., 1998; Laluraj, Thamban, & Satheesan, 2014; McConnell et al., 2007; Stohl & Sodemann, 2010). Consequently, Antarctic research can also provide opportunities to glean information regarding long-term changes in global climate or hemispheric circulation patterns (Elsässer et al., 2011; James, 1989; Kennicutt et al., 2015; Krinner, Petit, & Delmonte, 2010; Laluraj et al., 2014; Sinclair et al., 2013; Sinclair, Bertler, & Trompetter, 2010; Weller et al., 2011).

The type and concentrations of impurities observed in Antarctic snow, ice, or lower atmosphere depend upon the source emission intensity, the strength of lateral transport, vertical transport, and local influences (i.e., local production or transport from elsewhere in Antarctica) prevailing at the time (Wolff et al., 2008). Consequently, the fetch history of Antarctic air masses is a matter of multidisciplinary interest. While the underlying transport pathways of Antarctic pollutants have long been recognized (i.e., synoptic transport within the marine boundary layer or subsiding free tropospheric air; Bromwich & Parish, 1998; Chambers et al., 2014; Krinner et al., 2010; Kottmeier & Fay, 1998; Lambert, Ardouin, & Sanak, 1990; Li, Ginoux, & Ramaswamy, 2008; Polian et al., 1986; Pereira, 1990), some of the finer details of atmospheric transport mechanisms responsible for Antarctic aerosol deposition events remain elusive. For example, while numerous studies report simulated atmospheric transport to Antarctica from both hemispheres (e.g., Li et al., 2008; Mahowald et al., 1999, and references

therein), global climate models (GCMs) do not reliably reproduce key features of the seasonal cycle of atmospheric boundary layer concentrations of radon at coastal or inland Antarctic sites (e.g., Josse, Simon, & Peuch, 2004; Zhang et al., 2008). A corollary of this shortcoming is that GCMs do not faithfully represent all terrestrial influences on air that makes its way to Antarctica and that our understanding of these transport processes, or the way in which they can be most effectively parameterized, needs further refinement.

While back trajectories can assist with Antarctic fetch analysis, the paucity of observations in high southern latitudes, together with interpolations, parameterization simplifications, and the coarse spatial resolution of global model reanalysis products, can lead to large errors in fetch analysis (Harris, Draxler, & Oltmans, 2005; Parish & Cassano, 2001; Scarchilli, Frezzotti, & Ruti, 2011; Schlosser et al., 2008), particularly when integrated over traveltimes typical of advection between southern hemisphere continents and Antarctica. A more reliable and objective approach is to combine back trajectories with the constraints imposed by a suitable terrestrial tracer (e.g., Crawford, Zahorowski, & Cohen, 2009; Zahorowski et al., 2013).

Radon is a naturally occurring, unreactive gas with simple source-sink mechanisms that is frequently employed as a terrestrial tracer in transport and mixing studies (e.g., Dentener, Feichter, & Jeuken, 1999; Jacob et al., 1997; Koffi et al., 2016; Mahowald et al., 1997; Pereira et al., 2006; Rasch, Feichter, & Law, 2000; Zhang et al., 2008). Since radon has a half-life of 3.8 days it can provide unambiguous evidence of terrestrial influence on air within the past 2–3 weeks (Chambers et al., 2016; Zahorowski et al., 2013). In December 2015 a 1,200 L dual-flow-loop two-filter radon detector was installed at Jang Bogo Station (JBS), Terra Nova Bay, to complement observations made by a similarly designed 1,500 L detector at King Sejong Station (KSG), King George Island (Chambers et al., 2014).

Chambers et al. (2014) demonstrated that the temporal variation of radon concentrations in the boundary layer at KSG results from a combination of (i) Southern Ocean "baseline" air masses ($0.03 \leq Rn \leq 0.05$ Bq m^{-3}), (ii) rapid synoptically driven air mass transport from South America in the marine boundary layer (so-called "radonic storms") ($0.2 \leq Rn \leq 2.0$ Bq m^{-3}), (iii) local influences from exposed rock (which, at this site, typically enhance baseline radon concentrations by $\leq$0.05 Bq m^{-3}), and (iv) radon in tropospheric air subsiding at the pole (which, at this site, exhibited a seasonal cycle of amplitude ~0.05 Bq m^{-3}, characterized by a late summer maximum and spring minimum).

While radon proved to be an effective tool for air mass characterization at KSG, this low-lying island site, far removed from the Antarctic mainland (62°S), is not typical of most coastal Antarctic stations. Prior to embarking upon a complete seasonal analysis of air mass origins and characteristics at JBS, it is necessary to demonstrate the challenges and effectiveness of using radon as an atmospheric tracer at this complex site, sheltered behind Cape Adare and adjacent the foothills of the Transantarctic Mountains. Ultimately, the value of ongoing JBS radon observations will depend upon how well the concentration variability can be characterized and interpreted.

The aims of this study are therefore to (i) contrast the radon variability between KSG and JBS, (ii) characterize local Antarctic radon emissions from exposed rock, (iii) compare typical fetch regions of the two sites, (iv) develop a technique to reliably distinguish between katabatic and oceanic (boundary layer) air masses at coastal east Antarctic sites, and (v) establish radon thresholds to identify baseline air masses at each site.

We focus this initial investigation on summer only because this period poses the greatest challenges for the radon tracer technique: the fraction of exposed ground is maximized, as is permafrost depth, resulting in peak local radon emissions; wind speeds (between katabatic and other downslope wind episodes) are often light, exacerbating local radon source influences; and katabatic flow velocities are at their seasonal minimum, making it more challenging to reliably distinguish them from other high-velocity events (such as the Ross Ice Shelf Airstream (RAS) and other barrier winds; Coggins & McDonald, 2015; Steinhoff, Chaudhuri, & Bromwich, 2009). In addition, other direct radon observations made earlier at each site (using an independent technique; Pereria & da Silva, 1989) are available in this season for comparisons.

2. Methods

2.1. Sites and Overview

We report on the first summer (December 2015 to February 2016) of atmospheric radon measurements at Jang Bogo Station made collaboratively by the Korea Polar Research Institute (KOPRI) and the Australian

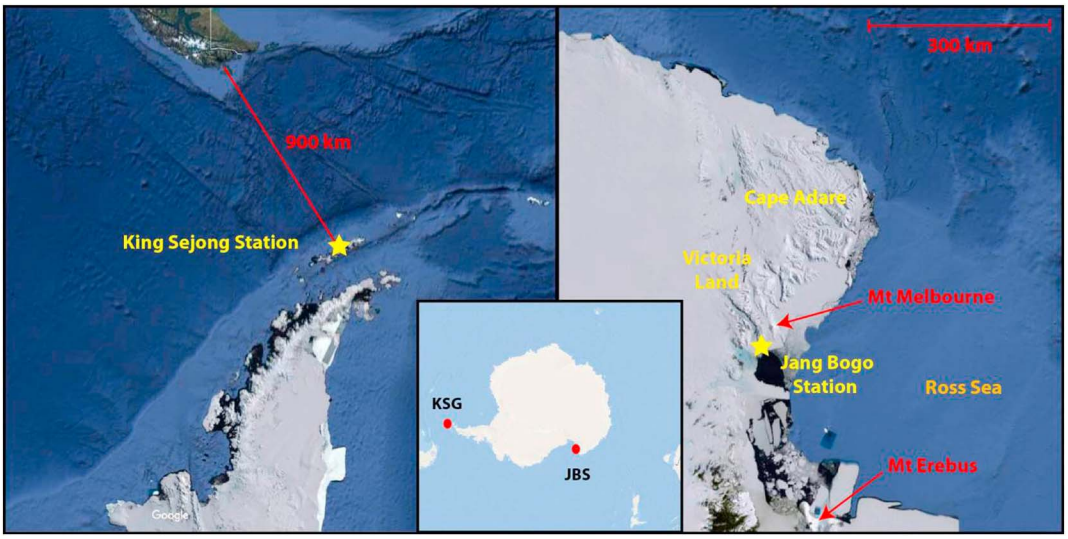

Figure 1. Relative locations of King Sejong and Jang Bogo stations on the Antarctic mainland. Images sourced from Google Maps and Microsoft Encarta Reference Library 2008.

Nuclear Science and Technology Organisation (ANSTO). Results are compared with simultaneous observations from King Sejong Station, in a contrasting location (Figure 1).

JBS radon measurements commenced on 15 December 2015. The station is on a peninsula between the Campbell and Priestley glaciers in Terra Nova Bay (74.623°S, 164.228°E; 10 m above sea level), on the west coast of the Ross Sea. An Italian base, Mario Zucchelli Station (MZS), lies 10 km SSW (see Figure 4b). Adjacent the site to the west are the Transantarctic Mountains, reaching more than 2,000 m within 50–100 km of the coast. There are several active volcanoes in the vicinity of JBS, including Mount Melbourne (30 km NE) and Mount Erebus (350 km SSE). A comprehensive climatology of the region has been provided by Coggins, McDonald, and Jolly (2014). Typically, however, summer is characterized by light winds, interspersed by katabatic drainage events (e.g., Bromwich & Liu, 1996).

KSG radon measurements commenced on 10 February 2013. A detailed description of this site and radon observations has been provided by Chambers et al. (2014).

2.2. Meteorology and Radon Observations

JBS meteorological observations were made from a 10 m tower ~170 m northwest of the radon detector. Instrumentation included a 2-D sonic anemometer (WMT700, Vaisala; 10 m above ground level (agl)), temperature and humidity probe (HMP155, Vaisala; 1.8 m agl), and a barometer (PTB330; 1.3 m agl). Wind data were sampled every 3 s and the other parameters every minute, which were then stored as 10 min averages on the data logger (QML201, Vaisala). All observations were then aggregated to hourly values in postprocessing, such that the timestamp marked the start of the observation period, from which absolute humidity values were derived. For reference purposes, wind speed, direction, and pressure at King Sejong station were recorded at 10 m agl and temperature/relative humidity recorded at 1.5 m agl.

Direct, continuous radon measurements were made using a 1,200 L two-filter dual-flow-loop radon detector custom built by ANSTO. Operational characteristics were similar to the 1,500 L KSG radon detector (Chambers et al., 2014). The detector was installed in the autosonde building, ~40 m east of the main station. Air is sampled at 55 L min^{-1} through 50 mm high-density polyethylene pipe from ~6 m agl. A 400 L delay volume is incorporated within the sampling line to prevent thoron (^{220}Rn; $t_{0.5}$ = 55.6 s) contamination of the sampled air.

The detector is calibrated monthly using a Pylon ^{226}Ra source (9.669 ± 0.122 kBq) traceable to National Institute of Standards and Technology standards. The detector's sensitivity was 0.32 c/s/Bq m^{-3} (coefficient of variability 2.0%). Instrumental background is checked quarterly and was 0.89 c min^{-1} at the time of commissioning. The detector's lower limit of determination (the radon concentration at which the

counting error exceeds 30% for a 1 h count) is 0.03 Bq m^{-3}. This uncertainty reduces with increasing radon concentration (<10% at concentrations of 0.1 Bq m^{-3} for a 1 h count) and drops off as ~$N^{-1/2}$ for N consecutive hourly samples.

All times reported are local times, and the southern hemisphere definition of summer has been adopted (December–February).

2.3. Back Trajectories and Cluster Analysis

Hourly 10 day back trajectories were calculated using the PC version of HYSPLIT v4.0 (Hybrid Single-Particle Lagrangian Integrated Trajectory; Draxler & Rolph, 2003). Calculations were based on meteorological data of 1° × 1° resolution generated by the Global Data Assimilation System model run by the National Weather Service's National Centers for Environmental Prediction (NCEP) (Kalnay et al., 1996). Based on estimated daytime mixing depths for the regions (section 3.2), starting heights of 300 m and 200 m were used for KSG and JBS trajectories, respectively. From the full database of 10 day back trajectories, subsets of 3 and 5 day trajectories were extracted for subsequent analyses.

Composite mean sea level pressure (MSLP) charts in section 3.5 were calculated using sea level pressure from the ERA-Interim Reanalysis (provided on a 0.75° × 0.75° grid at 3 h time intervals; Dee et al., 2011); only the midnight values were used.

Cluster analyses (section 3.4) were also performed using HYSPLIT, based on two 3 day back trajectories per day (00 and 12 UTC). Details regarding the HYSPLIT k-means clustering algorithm are provided by Stein et al. (2015, and references therein), Draxler et al. (2016), and at the ARL NOAA site ready.arl.noaa.gov/HYSPLIT.php. Briefly, with this method, each trajectory is initially considered to be a separate cluster. A number of iterations are then carried out within which pairs of clusters are combined. Determination of which two clusters to combine is made based on the cluster total spatial variance (TSV). TSV is determined by (i) calculating the cluster's mean trajectory, (ii) calculating the sum of the squared differences between each trajectory and the cluster's mean trajectory (i.e., the cluster spatial variance; SPVAR), and then finally (iii) calculating the sum of all SPVARs within a cluster. The pair of clusters with the smallest TSV is combined. Iterations continue until all clusters have been grouped into a single cluster. The optimal number of clusters can be determined from a plot of percent change in TSV against the number of remaining clusters. Typically, one of the late iteration steps will result in a particularly large increase in %ΔTSV, indicating that "different," rather than "similar," clusters are being paired. The number of clusters chosen to display is derived from the iteration prior to the step change in TSV.

3. Results

3.1. Overview of Antarctic Radon Characteristics

The summer-average KSG radon concentration was 0.063 ± σ0.031 Bq m^{-3}, typical of a marine baseline site (e.g., Polian et al., 1986; Zahorowski et al., 2013); however, the corresponding JBS value was an order of magnitude higher (0.94 ± σ0.74 Bq m^{-3}). By comparison, Tositti et al. (2002) reported summer-mean concentrations at Ferraz (King George Island; Figure 4a) of 0.11 Bq m^{-3}, and at MZS of 0.51 Bq m^{-3}. More recently (summer 2001–2002), a mean concentration of 0.65 ± σ0.64 Bq m^{-3} was observed at MZS.

Summer KSG and JBS radon concentrations were substantially higher than values reported for the coastal site Neumayer (0.028 ± σ0.013 Bq m^{-3}; Weller et al., 2014). However, there is little exposed rock around Neumayer (Weller et al., 2002). In fact, summer radon concentrations at Neumayer were more comparable to values observed inland at Dome C (0.02 ± σ0.01 Bq m^{-3}; S. Preunkert, personal communication), where there is also little exposed rock nearby.

3.1.1. Radon Time Series

The contrasting physical settings of KSG (Antarctic fringe island site) and JBS (East Antarctic coastal site) result in vastly different radon characteristics (Figure 2). A logarithmic scale was chosen here to demonstrate the range of concentrations more clearly.

KSG radon concentrations were characterized by occasional sharp peaks (to ~0.3 Bq m^{-3}) rising from a low baseline value (0.02–0.04 Bq m^{-3}), similar to observations by Polian et al. (1986), Balkanski and Jacob (1990), and Pereira (1990). JBS radon concentrations, on the other hand, represented a mixture of low, moderate, and

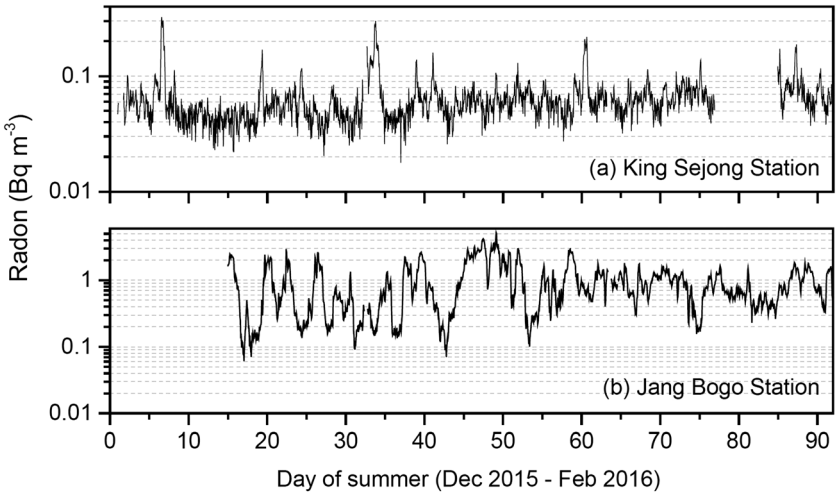

Figure 2. Hourly radon measurements at KSG and JBS throughout summer 2015–2016.

high values (ranging from 0.06 to 5.2 Bq m^{-3}) without a well-defined baseline concentration, indicating a highly variable degree of terrestrial influence on air masses. Given that JBS is 3,000–4,000 km from the nearest nonpolar southern hemisphere continent, compared to only 900 km for KSG, this result is counterintuitive if the common assumption of a negligible Antarctic radon source function is made (Elsässer et al., 2011; Jacob et al., 1997; Lambert et al., 1990; Zhang et al., 2008).

Although the JBS radon concentrations were higher than at KSG or numerous other Antarctic stations including Mawson, Neumayer, and Dumont d'Urville (e.g., Chambers et al., 2014; Lambert et al., 1990; Polian et al., 1986; Weller et al., 2014), observations agreed well with summer values at nearby MZS (0 to 5.4 Bq m^{-3}; e.g., Figure 5a of Tositti et al., 2002), which had a frequency distribution closely matching Figure 3b.

To put the KSG and JBS observations into perspective regarding recent terrestrial influence on air masses, air masses in long-term (≥2 weeks) equilibrium with the Southern Ocean have radon concentrations between 0.03 and 0.05 Bq m^{-3} (Zahorowski et al., 2013). Furthermore, a threshold of 0.1 Bq m^{-3} is often employed as an indicator of recent terrestrial influence (e.g., Molloy & Galbally, 2014). By these standards, 94% of KSG air masses had not experienced recent terrestrial influence (Figure 3a). Conversely, only ~1% of JBS air masses were free of significant recent terrestrial influence (Figure 3b). The primary reason for this contrast is that KSG is situated on the fringes of the Antarctic mainland, surrounded by ocean, whereas JBS is at the foothills of the Transantarctic Mountains with limited direct access to the open Southern Ocean (Figure 1), and proximal to several active volcanoes (Tositti et al., 2002).

While there is snow-free land near both stations in summer (Figure 4), at JBS there is additional exposed land north and south (along the foothills of the mountains), with rocky outcrops that are kept mostly free of snow year-round by downslope winds (Tositti et al., 2002). RAS events and other barrier winds often bring air

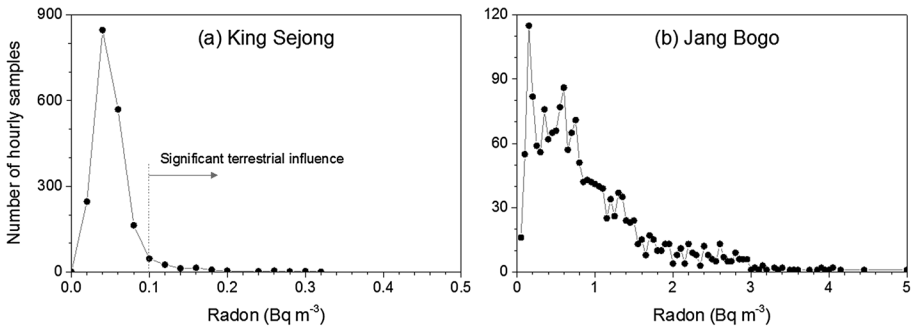

Figure 3. Frequency distributions of hourly radon concentrations at JBS and KSG.

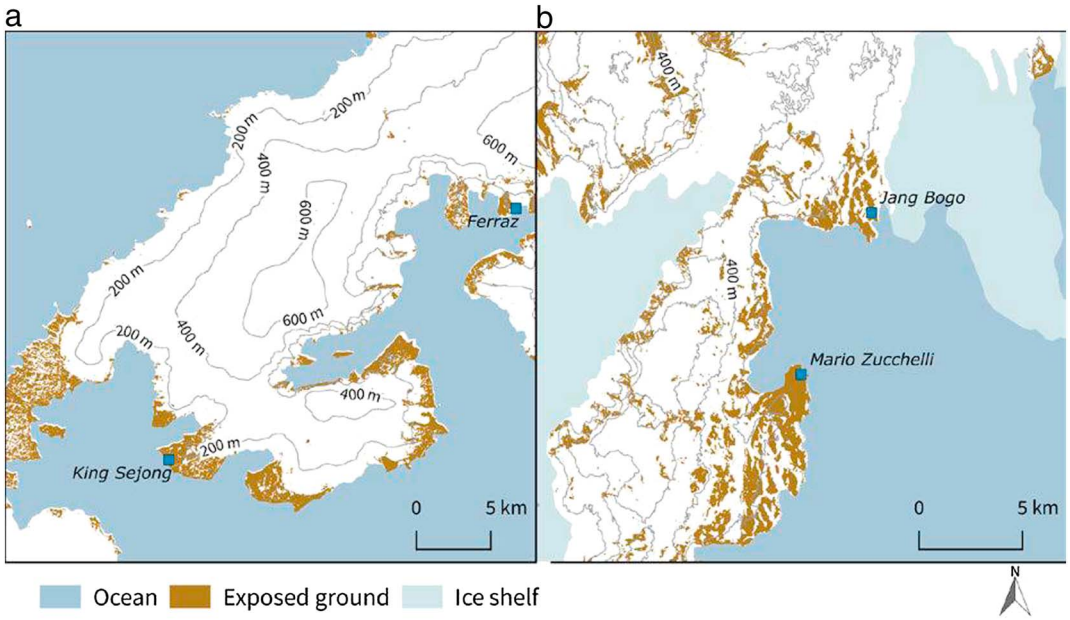

Figure 4. Close-up views of KSG (a) and JBS (b) including topography and exposed land. Topography sources: Braun, Betsch, and Seehaus (2016) and ASTER GDEM (a product of METI and NASA). Land type definitions from the Antarctic Digital Database (http://www.add.scar.org/). Exposed land is from the rock outcrop map of Burton-Johnson et al. (2016). Prevailing summer wind directions at KSG and JBS were approximately west, and southwest, respectively. Refer to Figure 1 for site locations relative to mainland Antarctica.

masses from these regions to JBS (Steinhoff et al., 2009). Information regarding rock type and weathering, Radium-226 content, and radon emanation near KSG and JBS is provided by Evangelista and Pereira (2002) and Tositti et al. (2002). Weathering increases the rock surface area exposed to the atmosphere, which in turn increases radon emission. Tositti et al. (2002) also point out significant fumarole activity in the vicinity of Mount Melbourne and Mount Erebus. Subterranean gases can attain very high radon concentrations, resulting in high local radon concentrations after venting events. Back trajectories (not shown) directly linked most JBS radon events $\geq$4 Bq m^{-3} (Figure 3b) to emissions from active volcanic regions. Furthermore, atmospheric mixing depths are typically lower at JBS than KSG (sometimes by a factor of 2–3), resulting in a concentration of local radon emissions.

3.1.2. Radon Variability: Diurnal Time Scale

Little diurnal variability in radon concentrations was observed at either site (Figure 5). Both median and mean diurnal cycles at KSG are characterized by morning maximum and late afternoon minimum values, as typical of an inland site, but with an amplitude of only around 0.005 Bq m^{-3} (3 orders of magnitude less than for a typical inland site), indicative of a dominant marine influence. Comparing mean to median values indicates a slight skewness ($<$10% from median) resulting from local influences on radon concentrations at low wind speeds.

At JBS median radon concentrations peaked between 0400 and 0600 h (during peak downslope wind conditions; see Figure 6a), and again in the early evening when wind directions were often from the NE (across the flanks of Mount Melbourne that are least snow covered, and also the direction of the more distant coastline of Cape Adare). Minimum concentrations occurred in the midafternoon, associated with a change in wind direction to ENE, and again between 2200 and 0200 h when flow was often coming down from the Campbell Glacier. Comparing the mean to the median JBS diurnal radon cycles indicates a substantial skewness (~30% from median) due to local influences on radon concentrations. The skewness is greatest between 1000 and 2000 h when local flow was often *along* the Transantarctic Mountains. Diurnal mean radon concentrations are low between 2200 and 0200 h when local flow is often down the Campbell Glacier and exhibit a secondary maximum between 0300 and 0700 h when katabatic flow is common and most pronounced.

Tositti et al. (2002) reported no diurnal cycle at Ferraz but a diurnal cycle in hourly mean values at MZS characterized by a morning maximum and afternoon minimum (amplitude of ~0.6 Bq m^{-3}). The reason for the difference in diurnal cycles of radon between MZS and JBS is presently unknown but will be investigated

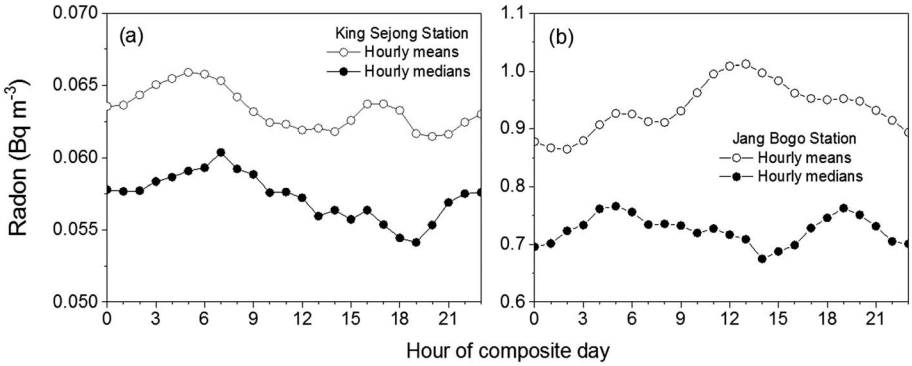

Figure 5. Hourly mean and median diurnal composite radon concentrations at KSG and JBS in summer. Due to the small concentration range at KSG values have been smoothed using a 3-point running mean.

further when the data set has been extended. Most likely it is related to the increased amount of exposed ground in the vicinity of MZS compared to JBS as evident in Figure 4b.

To assist with interpretation of the KSG and JBS diurnal radon cycles, we investigated the site meteorology (Figure 6). Compared to JBS, the amplitudes of KSG meteorological diurnal cycles were damped, modulated by a stabilizing oceanic influence. At JBS, early mornings (0400–0700 h) were characterized by higher wind speeds, a sharp drop in temperature, and low humidity. Furthermore, wind direction changed to 280–330° between 0000 and 1100 h (Figure 7), corresponding to the bearing of a local topographic maximum (Figure 4b). These observations are consistent with downslope flow, some of which would be katabatic in nature and fed by subsidence of dry tropospheric air (Bromwich et al., 1993). As shown in Figure 4b, topography at JBS generally raises WNW of the site. Specifically, however, within 500–700 m of the meteorological tower, there are two small valleys in the flanks of the larger mountainside: one at a bearing of 280° and the other at a bearing of 310°. Consequently, the direction of downslope winds at this station tends to vary between these bearings.

Under downslope flow conditions (whether of katabatic or synoptic origin), the air has less opportunity for terrestrial influence and, since this air is faster moving on average (Figure 6a), would transit more rapidly over the 50–100 km of partially exposed ground directly upslope of the station (i.e., it would have less time to accumulate radon than air masses moving slowly along the coast for hundreds of kilometers). This is most likely the reason that the morning (0500–0600 h) peak in JBS mean radon concentration (Figure 5b) is less than the midday peak.

While there was little diurnal change in wind direction at KSG (Figure 7), a swing of ~135° from morning to afternoon was observed at JBS. With the cessation of morning katabatic flows, JBS wind direction typically swung around to 70–80° around noon, accompanied by a drop in wind speed (Figure 6a). This behavior was most prominent on low wind speed days when an intense anticyclonic system was southwest of JBS (see Figure 18a). Under these synoptic conditions the low-speed regional flow has a pronounced easterly component and dominates at times when the katabatic flow is not active.

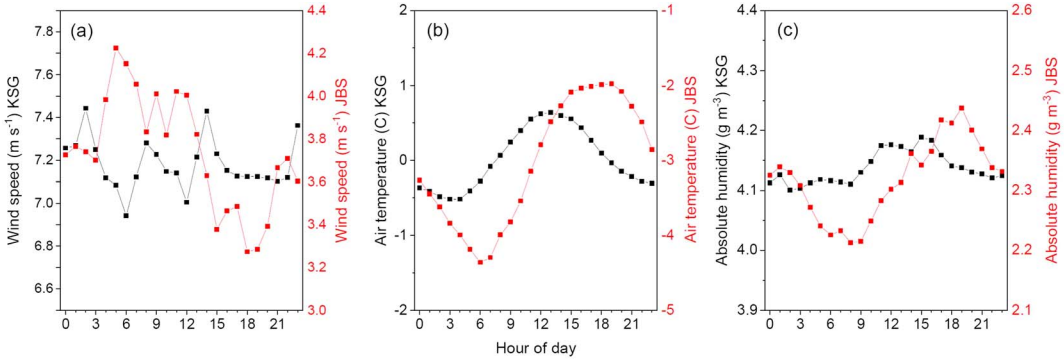

Figure 6. Diurnal composite wind speed, temperature, and absolute humidity at KSG and JBS for summer 2015–2016.

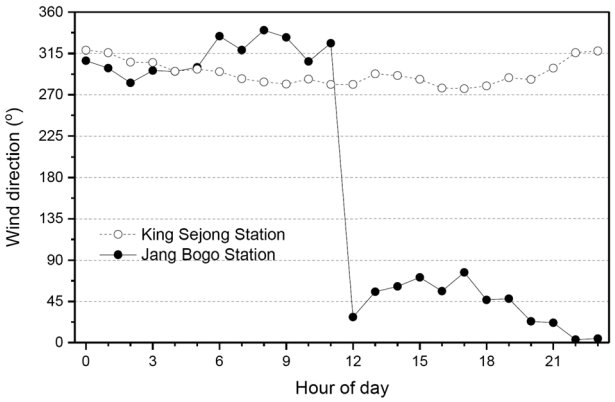

Figure 7. Comparison of diurnal wind directions at KSG and JBS in summer 2015–2016.

3.2. Local Source Contributions: Wind Speed Sampling Threshold

At most Antarctic bases anthropogenic emissions (from base activities) and natural emissions (from wildlife) can interfere with atmospheric observations (e.g., Wolff & Cachier, 1998). The relative contribution by local sources will depend upon (i) the source strength, (ii) atmospheric dilution (mixing depth and dispersion), and (iii) air mass contact time with the source. Determining sampling strategies to minimize such impacts is therefore very important. In areas where exposed rock is present, radon provides a convenient proxy for a constant, broadly distributed local source. Consequently, sampling techniques that minimize local radon contributions should also minimize contributions from other local sources (although sector exclusions may also be required for strong point sources).

Summer wind speeds were very different between KSG and JBS. While wind speed was almost normally distributed at KSG (mode 6 m s^{-1}), the JBS distribution was heavily skewed to low speeds (mode 1.5 m s^{-1}; Figures 8a and 8b). Behind Cape Adare (the northern side of which is one of the most prominent cyclogenesis regions in the Southern Hemisphere; Bromwich et al., 2011), summer wind speeds were often 0–3 m s^{-1}. These conditions represent near-stagnation in the western Ross Sea region. Typically, at this time of year, air moves north from the Ross Ice Shelf, channeled by the Transantarctic Mountains (Coggins & McDonald, 2015; Steinhoff et al., 2009), providing much opportunity to accumulate radon from regions of exposed ground. Wind speeds in excess of 3 m s^{-1} generally resulted from a combination of passing synoptic systems, RAS or other barrier wind events, and katabatic winds (Bromwich et al., 1993; Coggins et al., 2014; Coggins & McDonald, 2015; Steinhoff et al., 2009).

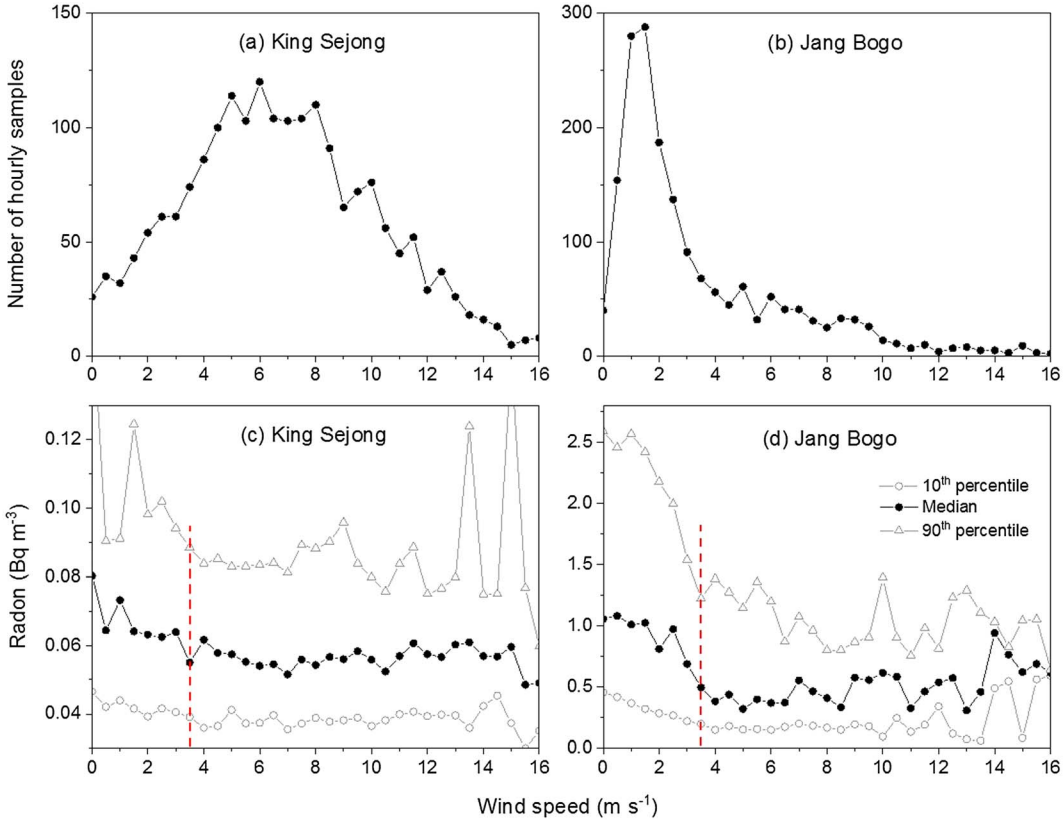

Figure 8. (a and b) Frequency histograms of hourly summer wind speed at KSG and JBS; (c and d) comparison of summer wind speed influence on radon concentrations at KSG and JBS.

To gauge the sensitivity of KSG and JBS observations to local radon emissions, we investigated the relationship between radon and wind speed. To do this, we allocated hourly samples to 0.5 m s^{-1} wind speed "bins" and calculated distributions (10th, 50th, and 90th percentiles) of the corresponding hourly radon concentrations (Figures 8c and 8d). Although some of the absolute differences between KSG and JBS can be attributed to atmospheric mixing depth, this has little impact on relative changes observed with wind speed. KSG experiences a marine-like boundary layer year-round (400–600 m; Chambers et al., 2014), whereas in summer JBS likely experiences mean mixing depths between 25 and 300 m (e.g., Angot et al., 2016; Jones et al., 2008; Parish & Bromwich, 2007). Another consideration is that activities of radium-226 are ~70% higher in rock near KSG than around JBS (Evangelista & Pereira, 2002; Tositti et al., 2002), but there is more exposed ground in the vicinity of JBS than KSG (see Burton-Johnson et al., 2016), and the rock is more weathered.

Generally, for inland continental sites, the greatest local contributions to near-surface observations occur for wind speeds <2 m s^{-1} (e.g., Chambers et al., 2015; Sesana, Caprioli, & Marcazzan, 2003). At KSG, the mean radon concentration for wind speeds <2 m s^{-1} was a factor of 1.22 higher than that for wind speeds between 5 and 10 m s^{-1}. At JBS, the mean radon for wind speeds <2 m s^{-1} was a factor of 2.35 higher than for wind speeds between 5 and 10 m s^{-1}. Based on the reduced radium content of rocks at JBS compared to KSG, the higher sensitivity of near-surface JBS radon concentrations to local influences (via reduced wind speed) is likely attributable to the greater amount of exposed ground near JBS (fumarole activity of active volcanoes in the vicinity of JBS may also play a role in some conditions).

To improve our ability to interpret KSG and JBS observations from remote or indirect transport events, it is instructive to know the wind speed threshold above which local influences are minimized. Based on the results of Figures 8c and 8d, a threshold of 3.5 m s^{-1} applies to both sites. However, only the wind speed distribution of KSG would enable the application of such a wind speed data exclusion threshold to eliminate local influences without significantly altering monthly statistics. At JBS the influence of local influences for future studies will need to be assessed on a case-by-case basis (and will be species specific) for all wind speeds below 3.5 m s^{-1}. This proposed threshold is higher than that proposed by Wolff and Cachier (Wolff & Cachier, 1998; 2.6 m s^{-1}), attributable to the higher resolution of our wind speed bins and broader distribution of local radon sources compared to the few point pollution sources discussed by Wolff and Cachier (1998).

Figures 8b and 8d highlight the wind speed influence and typically low JBS wind speeds, which explain much of the differences between the stations in Figure 2. Further evidence for strong local radon influences in the Terra Nova Bay area have been shown by the Rn-222 ($t_{0.5}$ = 3.8 days) to Rn-220 ($t_{0.5}$ = 56 s) ratios of Tositti et al. (2002).

3.3. Local Fetch Influences: Directional Dependence of Radon

At KSG, where South America is 900 km to the north, wind direction had a profound influence on radon (Figure 9a). The 90th percentile concentrations within the sector 340–50° were well-above marine baseline levels. For JBS, on the other hand, the nearest nonpolar continental fetch is 3,000–4,000 km away. Here the angular distribution of radon responded to local (Antarctic) influences. Immediately, SE of the station there is up to 540 m of semiexposed rock leading to the sea ice. Further from the station to the NE and SSW are the longest fetches of partially exposed rock. In addition, Mount Melbourne lies to the NE and Mount Erebus to the SE of the station (Figure 1b). Cape Washington, east of JBS across the Campbell Glacier, also influences JBS radon observations.

Based on median values, JBS radon concentrations were typically lowest when air masses arrived from 190 to 220° (Figure 9b), associated with extended oceanic fetch prior to passing over West Antarctica or the Ross Ice Shelf. Air arriving from 230 to 270° was associated with moderate to high speed flow that had been more directly steered by the local topography, resulting in intermediate radon concentrations. Slightly reduced median radon concentrations were observed from the downslope sectors (280–310°; red dashed box Figure 9b). While the high-speed downslope flows keep many rocky outcrops on the flanks of the Transantarctic Mountains free of snow (Tositti et al., 2002), the total fetch is only of order 50–100 km, and the high-speed winds reduce air mass travel times over the exposed ground compared to slower flow from the N through SE, which results in the highest concentrations.

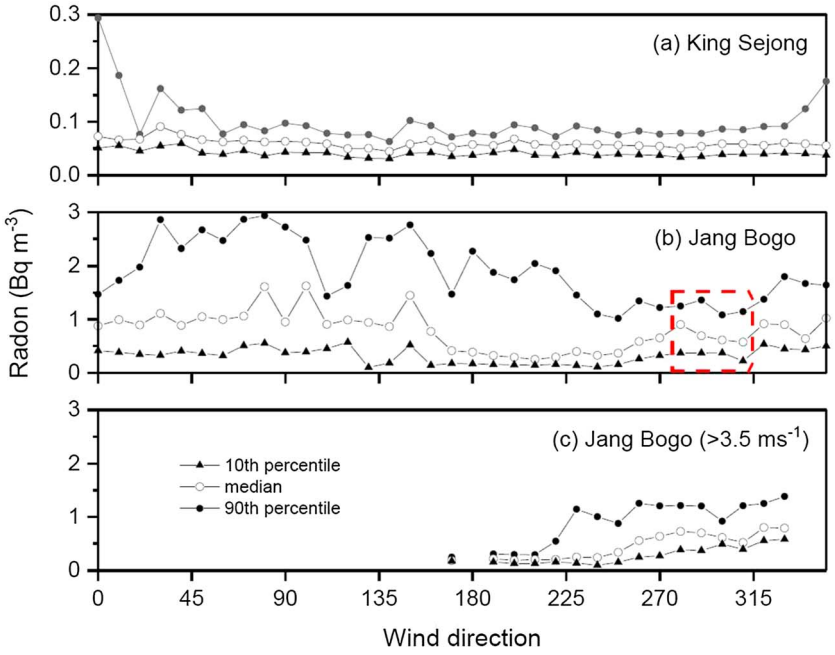

Figure 9. Angular distribution of hourly radon concentrations (10th, 50th, and 90th percentile distributions in 10° WD bins) at KSG and JBS. The dashed box indicates downslope wind sector.

To better indicate the influence of the lower speed air masses at JBS, Figure 9c is a reproduction of Figure 9b, but only including radon statistics for sectors which had more than 5 hourly events in summer associated with wind speeds >3.5 m s^{-1}. The low and tight radon distributions from 170 to 210° are associated with a strong oceanic signature (radon ~0.2 Bq m^{-3}), most likely Amundsen Sea-type air masses (see Figure 2 of Markle et al., 2012). Sinclair et al. (2013) and Bromwich and Liu (1996) also reported that air masses traversing West Antarctica had a typically "marine" signature. Flow from the sector 230–270° is likely the result of cyclonic disturbances in the Ross Sea region (e.g., Markle et al., 2012) that force air up against the

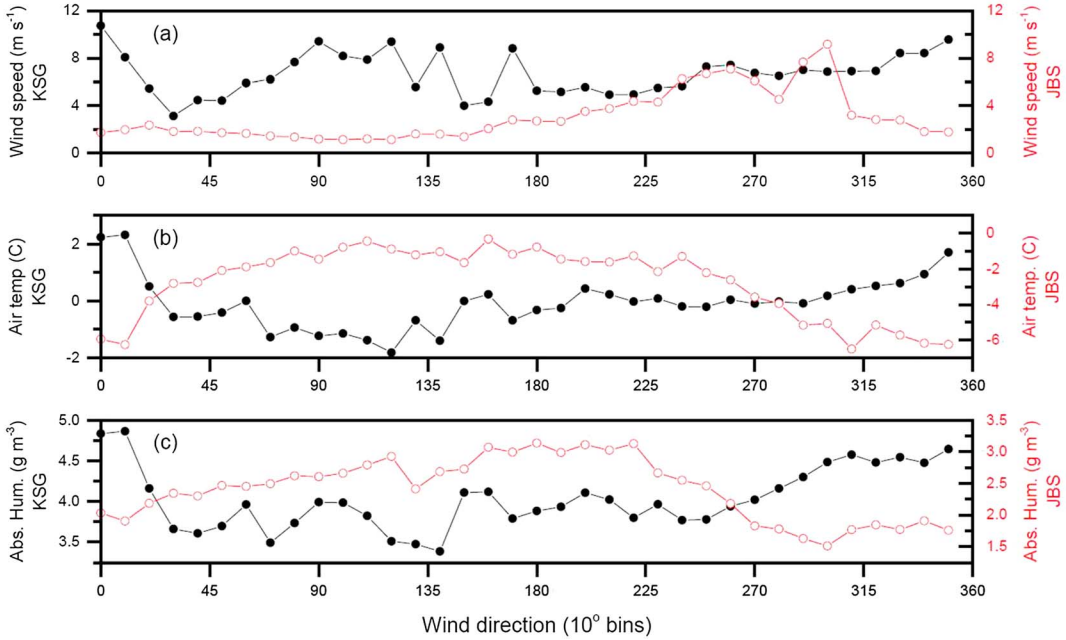

Figure 10. Angular distribution of wind speed, air temperature, and absolute humidity at KSG and JBS for summer 2015–2016.

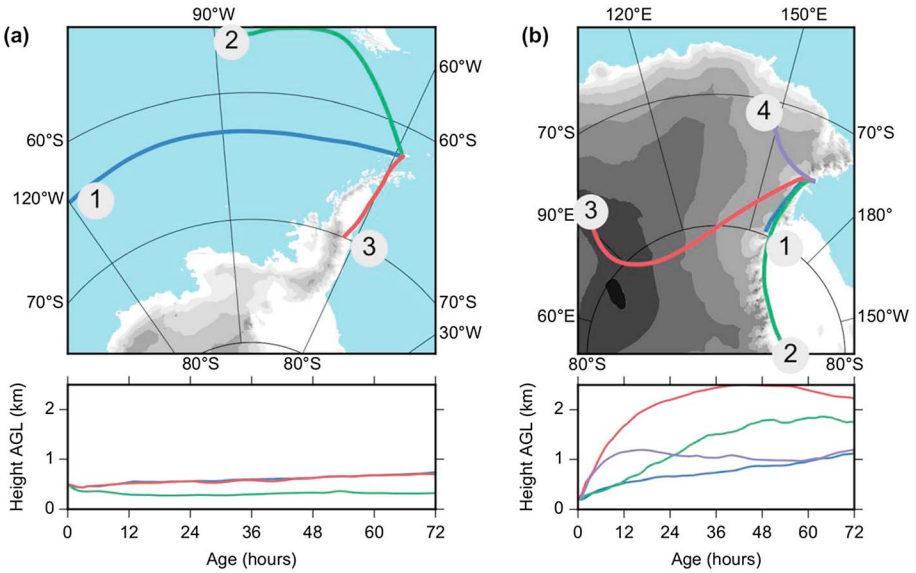

Figure 11. Clustered 3 day back trajectories for (a) King Sejong, and (b) Jang Bogo stations between December 2015 and February 2016. See text for details of cluster percentages. Antarctic topography (from ETOPO1; http://dx.doi.org/10.7289/V5C8276M) is shaded in 500 m intervals. Lower panels indicate air mass elevation at hour of hind-cast.

Transantarctic Mountains (median radon 0.3–0.6 Bq m^{-3}). For downslope winds (280–310°), median concentrations were 0.5–0.6 Bq m^{-3}.

Angular distributions of meteorological quantities (Figure 10) show a high wind speed bias at JBS between 160 and 330°, peaking at 290–300°. The stronger JBS winds between 160 and 270° are likely associated with RAS and other barrier wind events, whereas the fastest (and driest) air masses from 290° most likely represent katabatic winds (fed by tropospheric subsidence). At KSG the driest and coldest air masses (previously linked to subsidence events by Chambers et al., 2014), arrived from the SE, which was also a sector of high wind speeds.

3.4. Regional and Remote Air Mass Fetch

Based on a cluster analysis of twice-daily (00 and 12 UTC) summer 3 day back trajectories at each site (Figure 11), there were three main pathways by which air masses approached KSG: (1) 35% experienced long-term oceanic fetch (suitable for baseline studies), (2) 24% passed over or nearby South America, and (3) 41% traversed parts of continental Antarctica. As shown in the lower plot of Figure 11a, all of these air masses spent their last 3 days below 1,000 m agl.

Few JBS air masses had recent fetch outside of Antarctica in the first 3 days of hind-cast. Around 12% (#4) approached JBS from the northwest (Figure 11b), having been synoptically forced over Cape Adare to the station, 8% (#3) originated over the Antarctic interior and descended rapidly prior to reaching the site from the WSW (likely katabatic events), 63% (#1) were associated with slower moving flow pushed up against the Transantarctic Mountains (likely associated with the Ross Sea cyclonic events of Markle et al., 2012), whereas 17% (#2) traveled rapidly over the Ross Ice Shelf having likely originated in the Amundsen Sea. The fact that ~80% of trajectories had a strong southerly component is also consistent with the results of Steinhoff et al. (2009) and Coggins and McDonald (2015), who reported dominant southerly winds at JBS resulting from the weak and strong northern cyclonic regimes, the Ross Ice Shelf airstream, and other barrier winds.

Distributions of radon concentrations in the air masses associated with the trajectory clusters of Figure 11 are shown in Figure 12. For KSG the lowest of all concentrations were from air masses with extended oceanic fetch, the highest concentrations from South America, and the most consistent (compact distribution) from Antarctica. Median radon concentrations for extended oceanic fetch at KSG are higher than typical deep baseline marine values due to the 2–3 km of exposed land fetch west of the station, as shown in Figure 4a. For JBS the lowest radon concentrations were associated with the Amundsen Sea air masses coming in

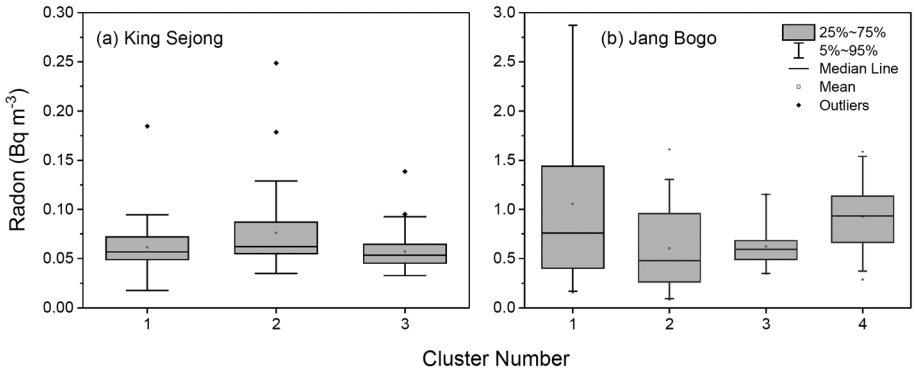

Figure 12. Radon concentration distributions for air masses arriving at (a) King Sejong and (b) Jang Bogo stations corresponding to the trajectory clusters of Figure 11.

from across the Ross Ice Shelf (#2), the highest concentrations from barrier flow up against the mountains (#1), and the most consistent (compact distribution) associated with katabatic drainage flows.

To a first approximation, there is little meridional flow at low altitudes to regions as far south as JBS in summer (Tositti et al., 2002). Li et al. (2008) and Krinner et al. (2010) show that the region is on the fringe of influence from Australia. In support of this, an analysis of hourly 10 day back trajectories (2,184 events) in summer identified only 11 trajectories (0.5%) that passed *close to* nonpolar southern hemisphere continents (Figure 13). When compared to the JBS radon observations, only 6 of these 11 events could be directly linked to recent terrestrial influence (radon peaks of 0.5–0.8 Bq m^{-3} above ambient; Figure 14). These peaks are of a similar magnitude to those discussed by Balkanski and Jacob (1990) at Kerguelen Island (4,200 km from South Africa). The mismatch between likely "hits" identified using trajectories alone, and those identified by radon, demonstrates the value of paired trajectory-tracer investigations for pollution studies in regions as remote as Antarctica.

Air masses associated with the dark blue trajectories of Figure 13 sweep down from the Southern Ocean and arrive in Antarctica near the eastern boundary of the Ross Ice Shelf. They then track across the ice shelf and meet the Transantarctic Mountains near the Byrd Glacier. From here they travel around 600 km north to the station guided by the flanks of the mountains, arriving at JBS with typically high locally -derived radon concentrations (Figure 14a).

Given that boundary layer radon concentrations for air masses leaving Australia are typically 2–4 Bq m^{-3} (e.g., Zahorowski et al., 2013), the observed remote continental perturbations in Figure 14a correspond to a decay time of 2–3 half lives, assuming minimal dilution. This closely corresponds to the 10 day back trajectory duration. These findings indicate that future JBS radon observations may be able to help characterize traveltime and dilution of pollution transport to the region from Australia and New Zealand.

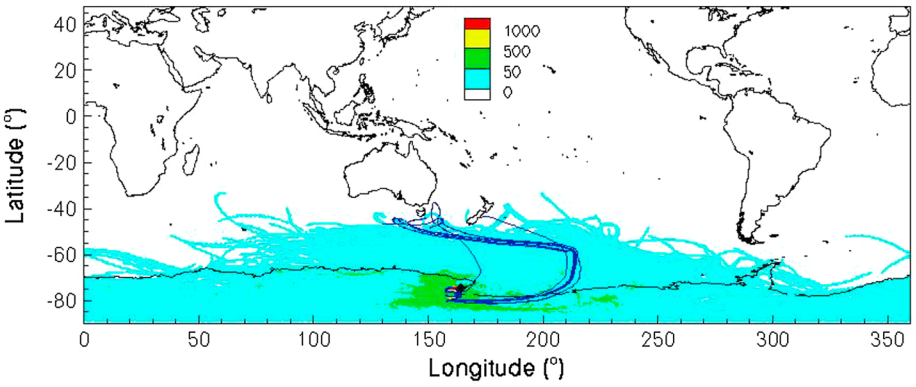

Figure 13. All hourly 10 day back trajectories from JBS in summer 2015–2016. The colors represent trajectory density. Trajectories passing closest to land shown in dark blue.

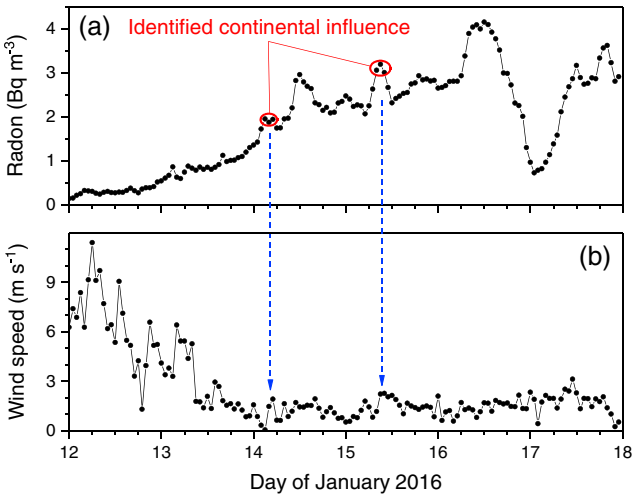

Figure 14. Examples of above background radon concentration peaks corresponding to continentally influenced back trajectories at JBS.

The low wind speeds (<3.5 m s^{-1}) associated with both remote continental transport events (Figure 14b) highlight the difficulty in assigning a wind speed threshold at JBS for the exclusion of possible local influences. For wind speeds <3.5 m s^{-1} at this site it may be necessary to rely primarily on wind direction and close visual inspection of pollutant time series to exclude local influences.

3.5. Identifying Katabatic Drainage Events

Elsässer et al. (2011) remarked upon the difficulty associated with reliably disentangling local, boundary layer, and tropospheric influences on continuous Antarctic observations; yet adequate characterization of Southern Ocean air masses, or pollution and nutrient transport pathways to Antarctic regions (as required; Kennicutt et al., 2015) is contingent on this skill. Having examined local influences in section 3.2, here we describe a technique that can be used to distinguish katabatic downslope wind events (originating from the troposphere or deep within the Antarctic interior) from long-term oceanic fetch within the marine boundary layer at coastal East Antarctic sites. Appropriately "tuned," this technique is also capable of discerning between downslope winds of katabatic origin and synoptically forced downslope winds, which can be problematic for other techniques (Parish & Cassano, 2001, 2003).

The overlap in Figure 10a between wind sectors influenced by stronger cyclonic synoptic systems (160–330°) and that most frequently influenced by downslope flow (280–310°) precludes the use of wind direction as a definitive indicator of downslope flow events. Of the downslope flow events, there is also a complete overlap of wind directions for events of a truly katabatic nature and those forced synoptically (Parish & Cassano, 2001, 2003). Furthermore, there is insufficient distinction between the wind speeds of summer downslope events (which are weaker than corresponding winter events; e.g., Bromwich et al., 1993; Bromwich & Liu, 1996) and the more vigorous cyclonic synoptic events for wind speed alone to be used as a definitive downslope event selection criterion. However, since katabatic winds (a subset of downslope winds) are typically fed by tropospheric subsidence, they are often associated with relatively dry air masses; also, they usually occur between 2200 and 0800 h.

Based on these characteristics, we used absolute humidity, together with a diurnal window within the period of typical katabatic flow, to distinguish katabatic drainage events and long-term oceanic fetch events, from other air masses arriving at the station. First, we high-pass filtered the hourly absolute humidity with a 2 week cutoff (to remove seasonal, but retain synoptic, influences). Then, for each day, we calculated the mean (filtered) absolute humidity between 0100 and 0600 h and sorted the resulting values (Figure 15).

Our selection technique is based on the premise that the most humid air masses arriving at JBS will have experienced the most consistent long-term oceanic fetch within the marine boundary layer prior to reaching Antarctica, and the driest air masses will have come to the station most directly from the Antarctic troposphere (most likely as a result of katabatic drainage flows). Air mass humidity values between these extremes will represent the full gamut of other possibilities (including, though not necessarily limited to oceanic air masses that have partially rained out, air masses that have been synoptically forced over portions of continental Antarctica or air masses that have been "lingering" around coastal regions of Antarctica).

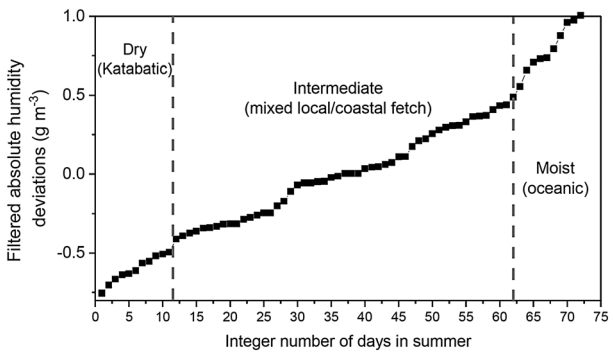

Figure 15. Sorted nocturnal mean (0100–0600 h window) filtered absolute humidity deviations at JBS in summer 2015–2016.

Based on the filtered absolute humidity values of Figure 15 at points of deviation from the gradually increasing trend of filtered absolute humidity for intermediate events, and consistent with the cluster analysis of Figure 11, we set a threshold value of the 14th percentile to identify katabatic events and the 80th percentile to identify oceanic events (shown by dashed vertical lines in Figure 15). It should be

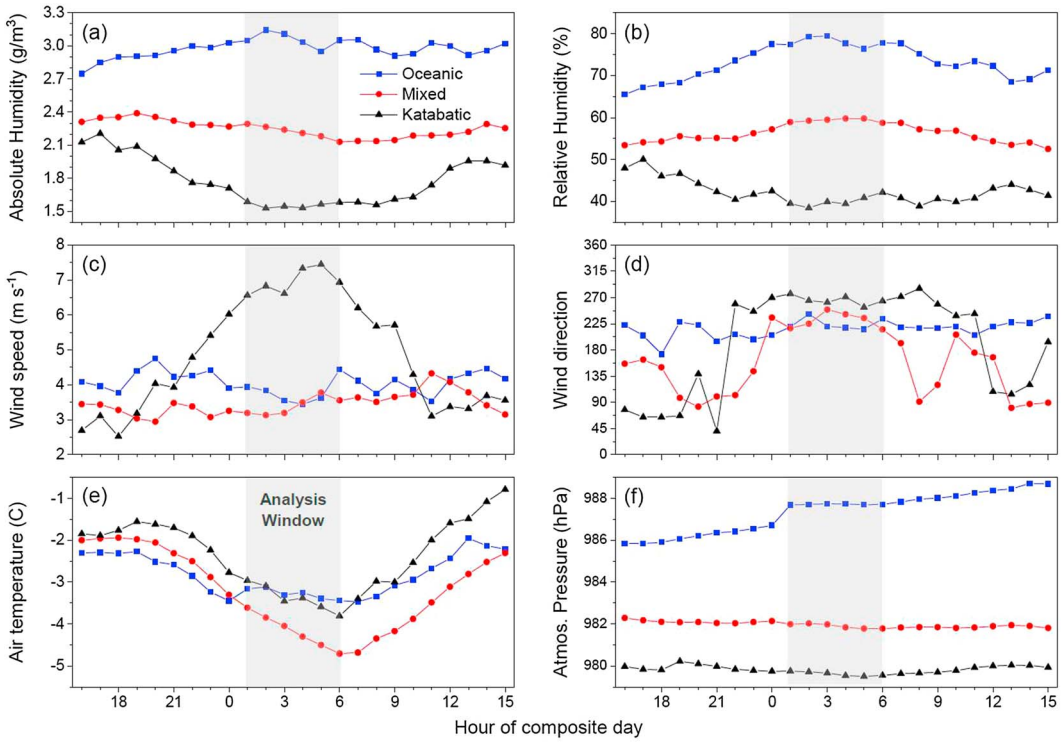

Figure 16. Diurnal composites of JBS meteorological parameters for katabatic, mixed, and oceanic events in summer 2015–2016 (note the shifted time axis). The shaded rectangle indicates 6 h event analysis window.

noted, however, that humidity threshold values for identifying katabatic and oceanic event conditions will be site specific. The remaining 66% of observations in this case are composed of mixed fetch conditions (local or coastal air masses), about which the approach outlined in this study can say little more.

Although our analysis of filtered absolute humidity was strictly performed using only 6 h of data each day (0100–0600 h), in order to provide some "synoptic context" to the conditions giving rise to the *katabatic*, *oceanic*, or mixed fetch events, here we apply the fetch category labels to whole 24 h periods. For this purpose we redefine our 1 day periods from 1600 h to 1500 h the next day (rather than midnight-to-midnight) to better focus on the *katabatic* event window, and then formed diurnal composites for events in each of our three categories, henceforth named *katabatic*, *mixed*, and *oceanic* (Figure 16). Since the targeted events are only guaranteed for the central 6 h of each diurnal window, "edge effects" (discontinuities from beginning to end) are sometimes evident in the composite diurnal cycles.

The influence of the selection process on the original (unfiltered) absolute humidity is evident in Figure 16a. The absolute humidity on days that katabatic flows occurred exhibited a pronounced diurnal cycle (in keeping with the intrinsic diurnal nature of katabatic flows), characterized by an afternoon maximum, and minimum values between 0100 h and 0800 h (during a time of pronounced katabatic flow) that were around half that of corresponding *oceanic* air masses. By comparison, only a very weak diurnal cycle was evident in the absolute humidity of mixed fetch events, and no consistent diurnal cycle was evident for days with predominantly oceanic fetch. This is consistent with mixed and oceanic fetch conditions being dictated by synoptic (as opposed to diurnal) timescale forcing. The diurnal cycle of relative humidity for mixed and oceanic fetch conditions was characterized by an afternoon minimum and nocturnal maximum, as expected given the influence of diurnal temperature changes on diurnal moisture contents that were relatively consistent. Conversely, the diurnal cycle of relative humidity on days containing katabatic events was completely out of phase (nocturnal minimum, daytime maximum).

Only days on which katabatic flow occurred exhibited a diurnal cycle of wind speed (Figure 16c), characterized by low values between 1100 and 1900 h, and maximum velocities between 0400 and 0500 h. For these days, wind directions were consistently 270–280° between 2200 and 0900 h, but switched to between NE-SE

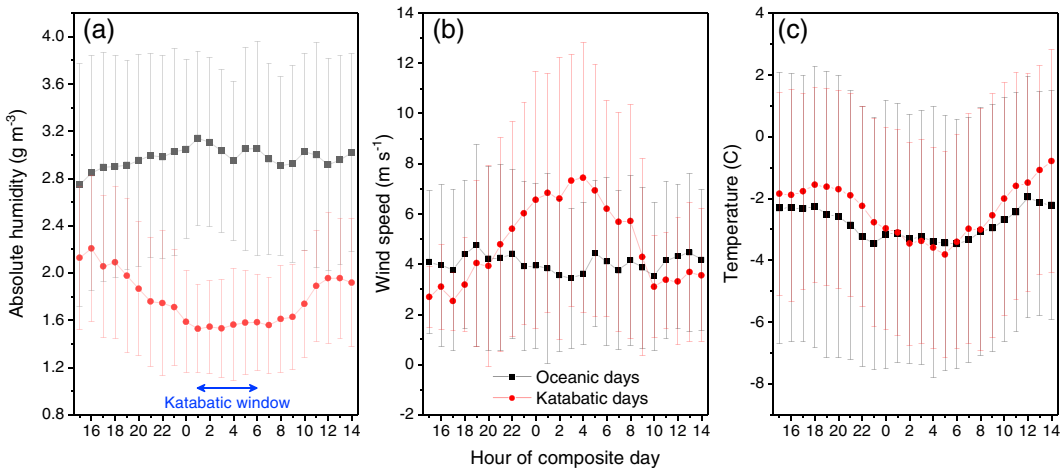

Figure 17. Hourly mean diurnal composites (with standard deviations) of absolute humidity, wind speed, and temperature for days with oceanic fetch and katabatic flow during the 6 h katabatic window period.

during the day (Figure 16d). The wind direction on days of predominantly oceanic fetch conditions was fairly consistently 200–225°.

Diurnal temperature amplitudes were greatest for katabatic event days, with minimum values between 0300 and 0700 h, and maximum values in the early afternoon, since these days were typically associated with anticyclonic, low gradient-wind conditions. Conversely, diurnal temperature amplitudes were smallest (damped) under the influence of extended oceanic fetch (Figure 16e).

Air pressure at JBS was low and relatively consistent for katabatic event days (Figure 16f), indicative of fairly stationary synoptic conditions. Conversely, oceanic fetch days were characterized by rapidly increasing pressures at JBS and mixed fetch days slowly decreasing pressure.

The efficiency with which our filtered absolute humidity technique distinguishes between oceanic and katabatic events within the identified 6 h katabatic window is shown in Figure 17. Within the katabatic window means and standard deviations of absolute humidity for oceanic and katabatic events are completely separate. Note that for other meteorological parameters, there is considerable overlap between values, rendering them less effective as event selection tools.

To demonstrate the underlying synoptic conditions driving each of the identified event categories, we formed composite midnight mean sea level pressure (MSLP) charts for each case; katabatic and oceanic day composites are shown in Figure 18. Conditions most conducive to the development of katabatic flows

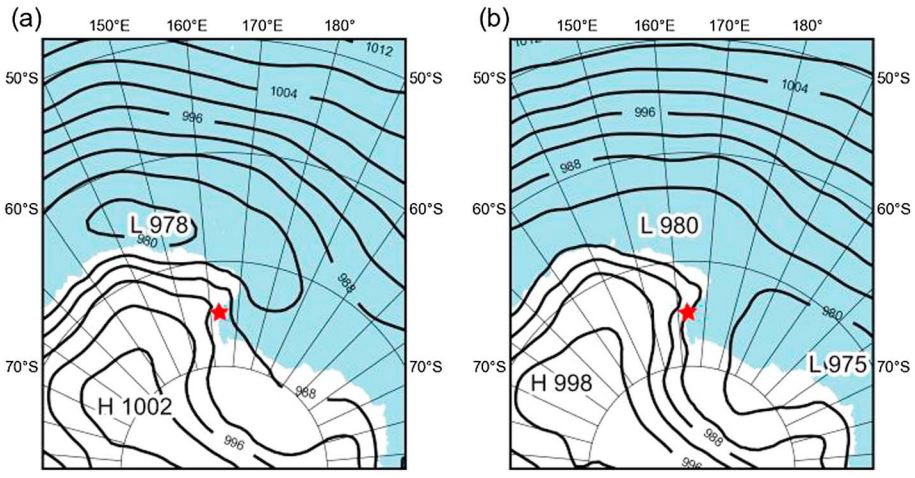

Figure 18. Composite 0000 h sea level pressure charts of the Jang Bogo region for (a) days experiencing katabatic flow conditions and (b) days dominated by long-term oceanic fetch conditions. The station location is marked by a red star.

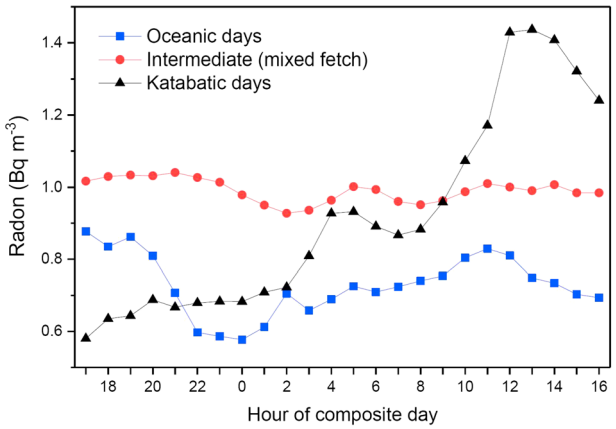

Figure 19. Diurnal composites of JBS radon concentrations for katabatic, intermediate and oceanic events in summer 2015–2016 (note the shifted time axis).

at "night" (time of low solar elevation) included an intense anticyclone over inland East Antarctica (SW of JBS) and a moderate intensity cyclonic system off the coast of Oates Land (Figure 18a). By comparison, conditions most conducive to extended oceanic fetch at JBS were characterized by a moderate anticyclone over inland East Antarctica, with an intense cyclonic system between the Amundsen and Ross Seas (Figure 18b). Depending on the exact location of the cyclonic system off Oates Land for katabatic event days, the synoptic wind field at JBS was light and varied between SE and NE flow. Under long-term oceanic fetch conditions, however, the synoptic winds were stronger and primarily from the SSW.

Diurnal cycles of radon for the three event categories (Figure 19) show that—within the 6 h analysis window—the slow-moving, mixed fetch events typically have the highest concentrations, and the oceanic events the lowest concentrations. Interestingly, katabatic events (during the period of peak katabatic flow 0400–0500 h) have relatively enhanced radon concentrations. This relative enhancement is likely attributable to a combination of two influences: (i) 50–100 km of fetch from the top of the Antarctic plateau with broken snow cover (Burton-Johnson et al., 2016) and (ii) an enhanced summer terrestrial influence on subsiding tropospheric air over Antarctica (e.g., Balkanski & Jacob, 1990; Chambers et al., 2014; Polian et al., 1986). The mismatch in radon concentration between the beginning and end of our katabatic event days is in part attributable to our application of an event categorization based on 6 h of observations to a full 24 h period. However, it also indicates that days when the strongest katabatic flows were observed usually followed periods of oceanic fetch (low radon concentration) and were calm and warm the following morning (leading to high radon concentrations as a result of large local radon influences). This is consistent with the observations shown in Figure 16.

3.6. Identifying Baseline Air

A primary function of radon observations at remote sites is to identify least terrestrially influenced (or baseline) air. Having minimized local influences at KSG using our 3.5 m s^{-1} wind speed threshold, here we define the radon threshold for baseline air as the monthly 10th percentile of the remaining observations (applying the wind speed threshold to JBS observations would have resulted in too few hourly observations to analyses, so this step was skipped). In future, characteristics of baseline air masses thus defined can be used as a reference to enable accurate quantification of pollution events from direct (synoptic) or indirect (via subsidence) transport to polar regions.

Baseline radon thresholds at KSG for December, January, and February were 0.034, 0.040, and 0.047 Bq m^{-3}, respectively. These values are similar to the 0.04 Bq m^{-3} radon concentration found by Zahorowski et al. (2013) at Cape Grim, for air masses in equilibrium with the Southern Ocean.

At JBS, radon concentrations within the oceanic and katabatic categories were considered separately. For *katabatic* events, only results from the 0400–0600 h window were considered (based on Figure 19). Monthly baseline thresholds are shown in Table 1. *Oceanic* baseline values at JBS were 3 to 9 times higher than monthly KSG baseline values, since these events typically approach from the SW-SSW having traveled close to the Transantarctic Mountains and over at least 1.3 km of exposed land adjacent the site (Figure 4b). Furthermore, mixing depths are shallower at JBS than KSG due to the cooler water temperatures and sea ice often present east and south of the station (enhancing radon concentrations).

Baseline threshold values for katabatic events at JBS were lower in December than later in summer, likely attributable to an increasing fraction of exposed ground on the flanks of the Transantarctic Mountains; a reasonable proxy for which maybe sea ice extent, which shows a rapid decline from October to March (Weller et al., 2014).

Table 1
Distributions (10th, 50th, and 90th Percentiles) of Hourly JBS Radon Concentrations (Bq m^{-3}) for Oceanic and Katabatic Events in December, January, and February

	Oceanic Fetch			Katabatic Events		
Month	10th	50th	90th	10th	50th	90th
Dec	0.18	0.98	1.86	0.11	0.92	2.15
Jan	0.15	0.23	2.08	0.36	1.27	1.44
Feb	0.20	0.78	1.03	0.32	0.60	1.06

Note. Uncertainty at 0.1 Bq m^{-3} is around 0.01 Bq m^{-3} and reduces for higher concentrations.

Interestingly, 90th percentile *katabatic* radon concentrations were similar to, or larger than, corresponding values for the oceanic fetch air masses, despite the shorter exposed land fetch down the flanks of the mountains as opposed to along the flanks of the mountains from the south. This may be indicative of a significant terrestrial signature in tropospheric air above Terra Nova Bay in summer, of the kind noted near KSG by Chambers et al. (2014). However, too little information is available on the amount of exposed rock along the katabatic fetch path leading to JBS to infer the magnitude of the tropospheric radon concentration in this region.

3.7. Constraining the Local Radon Flux

The first observations of radon fluxes from ice-free terrain in the King George Island region were made by Evangelista and Pereira (2002) during summer 1998/1999. The estimated average ^{222}Rn flux was 0.077 ± 0.048 atoms cm^{-2} s^{-1}, ranging between 0.002 and 0.28 atoms cm^{-2} s^{-1}, and the corresponding ^{220}Rn flux was 23 atoms cm^{-2} s^{-1}, based on a combination of two techniques: nuclear track detection and alpha spectrometry of radon daughters. It was found that the production of ^{222}Rn and ^{220}Rn by uranium (41.54 ± 7.17 Bq kg^{-1}) and thorium (57.97 ± 12.14 Bq kg^{-1}) equivalent soil contents, and a diffusion coefficient derived from experimental data for the local terrain, could account for this average flux. However, the large surges of atmospheric ^{222}Rn frequently observed in that area could not be explained by this flux but could be attributed to recent transport from South America.

En route to JBS, katabatic events traverse at least 50 km of ground with broken snow cover (e.g., Figure 4b). Focusing on the 0400–0600 h diurnal window of katabatic event days (guided by Figure 19), the distribution (10th, 50th, and 90th percentiles) of summer katabatic radon concentrations was 0.27, 0.98, and 1.48 Bq m^{-3}, respectively. The corresponding distribution of wind speed was 1.4, 5.7, and 13.7 m s^{-1}. Making the broad assumptions that (i) all katabatic events have a similar fetch region, (ii) most radon is accumulated locally (i.e., low tropospheric radon concentrations, C_{TROP} 0.05–0.1 Bq m^{-3}), (iii) the highest wind speeds (shortest accumulation times) are associated with the lowest radon concentrations, and vice versa, and (iv) the mixing depth of the katabatic flow under the low-wind-speed summer conditions is ~50 m (Angot et al., 2016; Jones et al., 2008), we can attempt to constrain the coastal Antarctic radon source function.

The change in radon concentration of a column of boundary layer air ($\Delta C = C_{JBS} - C_{TROP}$) is given by $\Delta C = \left(\frac{J\tau}{h}\right)$, where J is the radon flux, τ is the transit time, h is the boundary layer depth, and C_{TROP} is set to 0.1 Bq m^{-3}. So based on the 10th percentile wind speed and 90th percentile radon concentration, a lower bound on the average local radon flux is 0.09 atoms cm^{-2} s^{-1}. Conversely, using the 90th percentile wind speed and 10th percentile radon concentration, an upper bound on average local radon flux is 0.11 atoms cm^{-2} s^{-1}. These values are 9–11% of the global average terrestrial radon flux (Jacob et al., 1997) and in good agreement with the estimate of 0.077 atoms cm^{-2} s^{-1} for King George Island by Evangelista and Pereira (2002). The amount by which our radon flux estimates exceed those of Evangelista and Pereira (2002) may be indicative of summertime tropospheric radon concentrations in this region exceeding 0.1 Bq m^{-3} as a result of transport from midlatitude continents.

Wind profiles by Bromwich and Liu (1996) and Parish and Bromwich (2007) in the Terra Nova Bay region indicated a change in direction and initial peak speeds around 100 m agl. If these mixing depths are more typical of summer katabatic flow events (which are much slower than their winter counterparts) than our estimate above, the corresponding flux range would be 0.18–0.22 atoms cm^{-2} s^{-1}.

For north easterly air masses traveling down Cape Adare to JBS there is around 330 km of fetch (mainly frozen with numerous patches of exposed rock; Figure 1). At mean wind speeds of ~2 m s^{-1} (Figure 10a), this equates to a travel time of around 2 days. Within the first 10 km of transit (Shuttleworth, 1988) the atmospheric boundary layer would adjust from typically marine ($400 \leq Z_i \leq 600$ m) to typically Antarctic continental ($25 \leq Z_i \leq 300$ m) conditions. Assuming an average radon flux of 0.08 atoms cm^{-2} s^{-1} along this coastal fetch, and an average mixing depth of ~100 m, radon concentrations within the ABL at JBS could easily reach values of 2.5 Bq m^{-3}, which is in good agreement with Figure 3b. The few occasions on which JBS radon concentrations reach values of 3–5.2 Bq m^{-3} are therefore likely attributable to local volcanic influences or distant transport events (select cases were verified by back trajectory analysis).

While small, our estimated radon fluxes for coastal Antarctica are not negligible. Given the fraction of exposed ground around coastal Antarctica (Burton-Johnson et al., 2016), it may be important to include this source in the radon flux maps of global models.

4. Conclusions

We report on the first summer (December 2015 to February 2016) of measurements from a newly installed dual-flow-loop two-filter radon detector at Jang Bogo Station (Terra Nova Bay, Antarctica) and contrast them with simultaneous observations at King Sejong Station (King George Island, Antarctic Peninsula). Radon concentrations at KSG were characteristic of a marine baseline station (0.02–0.08 Bq m^{-3}, with occasional peaks to 0.3 Bq m^{-3}), whereas JBS values were highly variable (0.06–5.2 Bq m^{-3}), due to exposed coastal ground, shallow mixing depths, and local volcanic influences. Although Antarctic radon fluxes are frequently ignored, in summer we estimated that exposed ground near Terra Nova Bay has an average radon flux of 0.09–0.11 atoms cm^{-2} s^{-1}. These estimates of the coastal Antarctic radon source function, combined with the exposed land estimates of Burton-Johnson et al. (2016), could improve the accuracy of southern hemisphere radon simulations.

When cross-checked with radon, only half of the JBS 10 day back trajectories that were thought to have made contact with southern hemisphere continents showed signs of recent terrestrial influence, emphasizing the value of combined trajectory-tracer studies in this remote region. Radon in the Australian/New Zealand events was enhanced by 0.5–0.8 Bq m^{-3}, which indicates little dilution of the air mass en route to Antarctica based on typical terrestrial radon concentrations and the 10 day transit time.

A simple-to-implement technique (based on high-pass filtered absolute humidity with a 2 week cutoff) to distinguish between *katabatic*, *oceanic*, and *mixed fetch* (continental Antarctic) air masses at the meteorologically complex JBS site was developed and successfully trialed. When a longer-term data set is available for this site the event identification technique developed is expected to play a key role in addressing questions about the Antarctic atmosphere and global connections, and Southern Ocean influences, recently raised by Kennicutt et al. (2015). While humidity threshold values for event identification will be site specific, our preliminary analyses to date have indicated that this event selection technique can be applied without loss of generality to other coastal East Antarctic sites that experience regular katabatic flows. If direct, high-sensitivity atmospheric radon concentration observations were also available at these sites, air masses associated with long-term oceanic fetch or katabatic flow events could be further ranked according to an unambiguous relative scale of terrestrial influence.

Acknowledgments
This research was partly supported by KOPRI research grant (PE17010). We thank over-wintering staffs at Jang Bogo Station (Terra Nova Bay) and King Sejong Station (King George Island), Antarctica, as well as Ot Sisoutham and Sylvester Werczynski at the Australian Nuclear Science and Technology Organisation for their support of the radon measurement program at Jang Bogo Station. We also acknowledge NOAA Air Resources Laboratory (ARL) who made available the HYSPLIT transport and dispersion model and the relevant input files for the generation of back trajectories used in this paper. NCEP Reanalysis data, used in this work, were provided by the NOAA/OAR/ESRL PSD Boulder, Colorado. The data cited in this paper are available through PANGAEA: Data publisher for Earth and Environmental Science according to the AGU Data Policy at https://doi.pangaea.de/10.1594/PANGAEA.879451. Last but not least, we would like to acknowledge the efforts of the two anonymous reviewers whose detailed and considered feedback greatly improved the clarity of our findings.

References

Angot, H., Magand, O., Helmig, D., Ricaud, P., Quennehen, B., Gallée, H., … Dommergue, A. (2016). New insights into the atmospheric mercury cycling in central Antarctica and implications on a continental scale. *Atmospheric Chemistry and Physics*, *16*(13), 8249–8264. https://doi.org/10.5194/acp-16-8249-2016

Balkanski, Y. J., & Jacob, D. J. (1990). Transport of continental air to the subantarctic Indian Ocean. *Tellus B*, *42*(1), 62–75. https://doi.org/10.3402/tellusb.v42i1.15192

Barbante, C., Turetta, C., Gambaro, A., Capodaglio, G., & Scarponi, G. (1998). Sources and origins of aerosols reaching Antarctica as revealed by lead concentration profiles in shallow snow. *Annals of Glaciology*, *27*(1), 674–678. https://doi.org/10.3189/1998AoG27-1-674-678

Braun, M. H., Betsch, T., & Seehaus, T. (2016). King George Island TanDEM-X DEM, link to GeoTIFF. Institut für Geographie, Friedrich-Alexander-Universität, Erlangen-Nürnberg, PANGAEA. https://doi.org/10.1594/PANGAEA.863567

Bromwich, D. H., & Liu, Z. (1996). An observational study of the katabatic wind confluence zone near Siple Coast, West Antarctica. *Monthly Weather Review*, *124*(3), 462–477. https://doi.org/10.1175/1520-0493(1996)124%3C0462:AOSOTK%3E2.0.CO;2

Bromwich, D. H., & Parish, T. R. (1998). Antarctica: Barometer of climate change. Report to the National Science Foundation from the Antarctic Meteorology Workshop, Madison, Wisconsin, June 1998, published November 1998.

Bromwich, D. H., Parish, T. R., Pellegrini, A., Stearns, C. R., & Weidner, G. A. (1993). Spatial and temporal characteristics of the intense katabatic winds at Terra Nova Bay, Antarctica. In D. H. Bromwich & C. R. Stearns (Eds.), *Antarctic Meteorology and Climatology: Studies Based on Automatic Weather Stations*, *Antarctic Research Studies* (Vol. 61, pp. 47–68). Washington, DC: American Geophysical Union. https://doi.org/10.1029/AR061p0047

Bromwich, D. H., Steinhoff, D. F., Simmonds, I., Keay, K., & Fogt, R. L. (2011). Climatological aspects of cyclogenesis near Adelie Land Antarctica. *Tellus A*, *63*(5), 921–938. https://doi.org/10.1111/j.1600-0870.2011.00537.x

Burton-Johnson, A., Black, M., Fretwell, P. T., & Kaluza-Gilbert, J. (2016). An automated methodology for differentiating rock from snow, clouds and sea in Antarctica from Landsat 8 imagery: A new rock outcrop map and area estimation for the entire Antarctic continent. *The Cryosphere*, *10*(4), 1665–1677. https://doi.org/10.5194/tc-10-1665-2016

Chambers, S. D., Hong, S.-B., Williams, A. G., Crawford, J., Griffiths, A. D., & Park, S.-J. (2014). Characterising terrestrial influences on Antarctic air masses using Radon-222 measurements at King George Island. *Atmospheric Chemistry and Physics*, *14*(18), 9903–9916. https://doi.org/10.5194/acp-14-9903-2014

Chambers, S. D., Williams, A. G., Conen, F., Griffiths, A. D., Reimann, S., Steinbacher, M., … Barnes, J. E. (2016). Towards a universal "baseline" characterisation of air masses for high- and low-altitude observing stations using radon-222. *Aerosol and Air Quality Research*, *16*(3), 885–899. https://doi.org/10.4209/aaqr.2015.06.0391

Chambers, S. D., Williams, A. G., Crawford, J., & Griffiths, A. D. (2015). On the use of radon for quantifying the effects of atmospheric stability on urban emissions. *Atmospheric Chemistry and Physics*, *15*(3), 1175–1190. https://doi.org/10.5194/acp-15-1175-2015

Coggins, J. H. J., & McDonald, A. J. (2015). The influence of the Amundsen Sea low on the winds in the Ross Sea and surroundings: Insights from a synoptic climatology. *Journal of Geophysical Research: Atmospheres*, *120*, 2167–2189. https://doi.org/10.1002/2014JD022830

Coggins, J. H. J., McDonald, A. J., & Jolly, B. (2014). Synoptic climatology of the Ross ice shelf and Ross Sea region of Antarctica: k-means clustering and validation. *International Journal of Climatology*, *34*(7), 2330–2348. https://doi.org/10.1002/joc.3842

Crawford, J., Zahorowski, W., & Cohen, D. D. (2009). A new metric space incorporating radon-222 for generation of back trajectory clusters in atmospheric pollution studies. *Atmospheric Environment*, *43*(2), 371–381. https://doi.org/10.1016/j.atmosenv.2008.09.073

Davis, D., Nowak, J. B., Chen, G., Buhr, M., Arimoto, R., Hogan, A., … McMurry, P. (2001). Unexpected high levels of NO observed at South Pole. *Geophysical Research Letters*, *28*(19), 3625–3628. https://doi.org/10.1029/2000GL012584

Dee, D. P., Uppala, S. M., Simmons, A. J., Berrisford, P., Poli, P., Kobayashi, S., … Vitart, F. (2011). The ERA-Interim reanalysis: Configuration and performance of the data assimilation system. *Quarterly Journal of the Royal Meteorological Society*, *137*(656), 553–597. https://doi.org/10.1002/qj.828

Dentener, F., Feichter, J., & Jeuken, A. (1999). Simulation of ^{222}radon using on-line and off-line global models. *Tellus B*, *51*(3), 573–602. https://doi.org/10.3402/tellusb.v51i3.16440

Draxler, R., Stunder, B., Rolph, G., Stein, A., & Taylor, A (2016). HYSPLIT4 user's guide version 4—last revision: February 2016. Retrieved from https://www.arl.noaa.gov/documents/reports/hysplit_user_guide.pdf

Draxler, R. R., & Rolph, G. D. (2003). Hybrid Single-Particle Lagrangian Integrated Trajectory (HYSPLIT), model. Retrieved from http://www.arl.noaa.gov/ready/hysplit4.html (last accessed September 2016).

Elsässer, C., Wagenbach, D., Weller, R., Auer, M., Wallner, A., & Christl, M. (2011). Continuous 25-yr aerosol records at coastal Antarctica. Part 2: Variability of the radionuclides ^{7}Be, ^{10}Be and ^{210}Pb. *Tellus B*, *63*(5), 920–934. https://doi.org/10.1111/j.1600-0889.2011.00543.x

Evangelista, H., & Pereira, E. B. (2002). Radon flux at King George Island, Antarctic Peninsula. *Journal of Environmental Radioactivity*, *61*(3), 283–304. https://doi.org/10.1016/S0265-931X(01)00137-0

Grannas, A. M., Jones, A. E., Dibb, J., Ammann, M., Anastasio, C., Beine, H. J., … Zhu, T. (2007). An overview of snow photochemistry: Evidence, mechanisms and impacts. *Atmospheric Chemistry and Physics*, *7*(16), 4329–4373. https://doi.org/10.5194/acp-7-4329-2007

Harris, J. M., Draxler, R. R., & Oltmans, S. J. (2005). Trajectory model sensitivity to differences in input data and vertical transport method. *Journal of Geophysical Research*, *110*, D14109.

Jacob, D. J., Prather, M. J., Rasch, P. J., Shia, R.-L., Balkanski, Y. J., Beagley, S. R., … Zimmermann, P. (1997). Evaluation and intercomparison of global atmospheric transport models using ^{222}Rn and other short-lived tracers. *Journal of Geophysical Research*, *102*(D5), 5953–5970. https://doi.org/10.1029/96JD02955

James, I. N. (1989). The Antarctic drainage flow: Implications for hemispheric flow on the Southern Hemisphere. *Antarctic Science*, *1*, 279–290.

Jones, A. E., Wolff, E. W., Salmon, R. A., Bauguitte, S. J.-B., Roscoe, H. K., & Anderson, P. S., … Worton, D. R. (2008). Chemistry of the Antarctic boundary layer and the Interface with snow: An overview of the CHABLIS campaign. *Atmospheric Chemistry and Physics*, *8*(14), 3789–3803. https://doi.org/10.5194/acp-8-3789-2008

Josse, B., Simon, P., & Peuch, V.-H. (2004). Radon global simulations with the multiscale chemistry and transport model MOCAGE. *Tellus B*, *56*(4), 339–356. https://doi.org/10.3402/tellusb.v56i4.16448

Kalnay, E., Kanamitsu, M., Kistler, R., Collins, W., Deaven, D., Gandin, L., … Joseph, D. (1996). The NCEP/NCAR 40-year reanalysis project. *Bulletin of the American Meteorological Society*, *787*, 437–470.

Kennicutt, M. C., Chown, S. L., Cassano, J. J., Liggett, D., Peck, L. S., Massom, R., … Sutherland, W. J. (2015). A roadmap for Antarctic and Southern Ocean science for the next two decades and beyond. *Antarctic Science*, *27*(01), 3–18. https://doi.org/10.1017/S0954102014000674

Koffi, E. N., Bergamaschi, P., Karstens, U., Krol, M., Segers, A., Schmidt, M., … Williams, A. G. (2016). Evaluation of the boundary layer dynamics of the TM5 model over Europe. *Geoscientific Model Development*, *9*(9), 3137–3160. https://doi.org/10.5194/gmd-9-3137-2016

Kottmeier, C., & Fay, B. (1998). Trajectories in the Antarctic lower troposphere. *Journal of Geophysical Research*, *103*(D9), 10,947–10,959. https://doi.org/10.1029/97JD00768

Krinner, G., Petit, J.-R., & Delmonte, B. (2010). Altitude of atmospheric tracer transport towards Antarctica in present and glacial climate. *Quaternary Science Reviews*, *29*(1-2), 274–284. https://doi.org/10.1016/j.quascirev.2009.06.020

Laluraj, C. M., Thamban, M., & Satheesan, K. (2014). Dust and associated geochemical fluxes in a firn core from coastal East Antarctica and its linkages with Southern Hemisphere climate variability over the last 50 years. *Atmospheric Environment*, *90*, 23–32. https://doi.org/10.1016/j.atmosenv.2014.03.031

Lambert, G., Ardouin, B., & Sanak, J. (1990). Atmospheric transport of trace elements toward Antarctica. *Tellus B*, *42*(1), 76–82. https://doi.org/10.3402/tellusb.v42i1.15193

Li, F., Ginoux, P., & Ramaswamy, V. (2008). Distribution, transport, and deposition of mineral dust in the Southern Ocean and Antarctica: Contribution of major sources. *Journal of Geophysical Research*, *113*, D10207. https://doi.org/10.1029/2007JD009190

Mahowald, N., Kohfeld, K., Hansson, M., Balkanski, Y., Harrison, S. P., Prentice, I. C., … Rodhe, H. (1999). Dust sources and deposition during the last glacial maximum and current climate: A comparison of model results with paleodata from ice cores and marine sediments. *Journal of Geophysical Research*, *104*(D13), 15895–15916. https://doi.org/10.1029/1999JD900084

Mahowald, N. M., Rasch, P. J., Eaton, B. E., Whittlestone, S., & Prinn, R. G. (1997). Transport of 222radon to the remote troposphere using the model of atmospheric transport and chemistry and assimilated winds from ECMWF and the National Center for EnvironmentalPrediction/NCAR. *Journal of Geophysical Research*, *102*(D23), 28,139–28,151. https://doi.org/10.1029/97JD02084

Markle, B. R., Bertler, N. A. N., Sinclair, K. E., & Sneed, S. B. (2012). Synoptic variability in the Ross Sea region, Antarctica, as seen from back-trajectory modeling and ice core analysis. *Journal of Geophysical Research*, *117*, D02113. https://doi.org/10.1029/2011JD016437

McConnell, J. R., Aristarain, A. J., Banta, J. R., Edwards, P. R., & Simões, J. P. (2007). 20th-Century doubling in dust archived in an Antarctic Peninsula ice core parallels climate change and desertification in South America. *PNAS*, *104*(14), 5743–5748. https://doi.org/10.1073/pnas.0607657104

Molloy, S. B., & Galbally, I. E. A. (2014). Identification of a suitable baseline definition of tropospheric ozone at Cape Grim, Tasmania. In N. Derek, P. B. Krummel, & S. J. Cleland (Eds.), *Baseline Atmospheric Program Australia 2009–2010*, *Australian Bureau of Meteorology and CSIRO Marine and Atmospheric Research* (pp. 7–16). Melbourne: Australian Bureau of Meteorology and CSIRO Marine and Atmospheric Research.

Parish, T. R., & Bromwich, D. H. (2007). Reexamination of the near-surface airflow over the Antarctic continent and implications on atmospheric circulations at high southern latitudes. *Monthly Weather Review*, *135*(5), 1961–1973. https://doi.org/10.1175/MWR3374.1

Parish, T. R., & Cassano, J. J. (2001). Forcing of the wintertime Antarctic boundary layer winds from the NCEP–NCAR global reanalysis. *Journal of Applied Meteorology*, *40*(4), 810–821. https://doi.org/10.1175/1520-0450(2001)040%3C0810:FOTWAB%3E2.0.CO;2

Parish, T. R., & Cassano, J. J. (2003). The role of katabatic winds on the Antarctic surface wind regime. *Monthly Weather Review*, *131*(2), 317–333. https://doi.org/10.1175/1520-0493(2003)131%3C0317:TROKWO%3E2.0.CO;2

Pereira, E. B. (1990). Radon-222 time series measurements in the Antarctic Peninsula (1986–1987). *Tellus B*, *42*(1), 39–45. https://doi.org/10.3402/tellusb.v42i1.15190

Pereira, E. B., Evangelista, H., Pereira, K. C. D., Cavalcanti, I. F. A., & Setzer, A. W. (2006). Apportionment of black carbon in the South Shetland Islands, Antarctic Peninsula. *Journal of Geophysical Research*, *111*, D03303. https://doi.org/10.1029/2005JD006086

Pereria, E. B., & da Silva, H. E. (1989). Atmospheric radon measurements by electrostatic precipitation. *Nuclear Instruments and Methods*, *A280*, 503–505.

Polian, G., Lambert, G., Ardouin, B., & Jegou, A. (1986). Long-range transport of continental radon in subantarctic and Antarctic areas. *Tellus B*, *38*(3-4), 178–189. https://doi.org/10.3402/tellusb.v38i3-4.15126

Rasch, P. J., Feichter, J., & Law, K. (2000). A comparison of scavenging and deposition processes in global models: Results from the WCRP Cambridge workshop of 1995. *Tellus B*, *52*(4), 1025–1056. https://doi.org/10.3402/tellusb.v52i4.17091

Scarchilli, C., Frezzotti, M., & Ruti, P. M. (2011). Snow precipitation at four ice core sites in East Antarctic: Provenance, seasonality, and blocking factors. *Climate Dynamics*, *37*(9-10), 2107–2125. https://doi.org/10.1007/s00382-010-0946-4

Schlosser, E., Oerter, H., Masson-Delmotte, V., & Reijmer, C. (2008). Atmospheric influence on the deuterium excess signal in polar firn: Implications for ice-core interpretation. *Journal of Glaciology*, *54*(184), 117–124. https://doi.org/10.3189/002214308784408991

Sesana, L., Caprioli, E., & Marcazzan, G. M. (2003). Long period study of outdoor radon concentration in Milan and correlation between its temporal variations and dispersion properties of atmosphere. *Journal of Environmental Radioactivity*, *65*(2), 147–160. https://doi.org/10.1016/S0265-931X(02)00093-0

Shuttleworth, W. J. (1988). Macrohydrology: The new challenge for process hydrology. *Journal of Hydrology*, *100*(1-3), 31–56. https://doi.org/10.1016/0022-1694(88)90180-1

Sinclair, K. E., Bertler, N. A. N., & Trompetter, W. J. (2010). Synoptic controls on precipitation pathways and snow delivery to high-accumulation ice core sites in the Ross Sea region, Antarctica. *Journal of Geophysical Research*, *115*, D22112. https://doi.org/10.1029/2010JD014383

Sinclair, K. E., Bertler, N. A. N., Trompetter, W. J., & Baisden, W. T. (2013). Seasonality of airmass pathways to coastal Antarctica: Ramifications for interpreting high-resolution ice core records. *Journal of Climate*, *26*(6), 2065–2076. https://doi.org/10.1175/JCLI-D-12-00167.1

Stein, A. F., Draxler, R. R., Rolph, G. D., Stunder, B. J. B., Cohen, M. D., & Ngan, F. (2015). Free access NOAA's HYSPLIT atmospheric transport and dispersion modeling system. *Bulletin of the American Meteorological Society*, *96*(12), 2059–2077. https://doi.org/10.1175/BAMS-D-14-00110.1

Steinhoff, D. F., Chaudhuri, S., & Bromwich, D. H. (2009). A case study of a Ross ice shelf airstream event: A new perspective. *Monthly Weather Review*, *137*(11), 4030–4046. https://doi.org/10.1175/2009MWR2880.1

Stohl, A., & Sodemann, H. (2010). Characteristics of atmospheric transport into the Antarctic troposphere. *Journal of Geophysical Research*, *115*, D02305. https://doi.org/10.1029/2009JD012536

Tositti, L., Pereira, E. B., Sandrini, S., Capra, D., Tubertini, O., & Bettoli, M. G. (2002). Assessment of summer trends of tropospheric radon isotopes in a coastal Antarctic Station (Terra Nova Bay). *International Journal of Environmental Analytical Chemistry*, *82*(5), 259–274. https://doi.org/10.1080/03067310290027767

Weller, R., Jones, A. E., Wille, A., Jacobi, H.-W., McIntyre, H. P., Sturges, W. T., … Wagenbach, D. (2002). Seasonality of reactive nitrogen oxides (NO_y) at Neumayer Station, Antarctica. *Journal of Geophysical Research*, *107*(D23), 4673. https://doi.org/10.1029/2002JD002495

Weller, R., Levin, I., Schmithüsen, D., Nachbar, M., Asseng, J., & Wagenbach, D. (2014). On the variability of atmospheric ^{222}Rn activity concentrations measured at Neumayer, coastal Antarctica. *Atmospheric Chemistry and Physics*, *14*(8), 3843–3853. https://doi.org/10.5194/acp-14-3843-2014

Weller, R., Wagenbach, D., Legrand, M., Elsasser, C., Tian-Kunze, X., & Konig-Langlo, G. (2011). Continuous 25-yr aerosol records at coastal Antarctica—I: Inter-annual variability of ionic compounds and links to climate indices. *Tellus B*, *63*(5), 901–919. https://doi.org/10.1111/j.1600-0889.2011.00542.x

Wolff, E. W., & Cachier, H. (1998). Concentrations and seasonal cycle of black carbon in aerosol at a coastal Antarctic station. *Journal of Geophysical Research*, *103*(D9), 11,033–11,041. https://doi.org/10.1029/97JD01363

Wolff, E. W., Jones, A. E., Bauguitte, S. J.-B., & Salmon, R. A. (2008). The interpretation of spikes and trends in concentration of nitrate in polar ice cores, based on evidence from snow and atmospheric measurements. *Atmospheric Chemistry and Physics*, *8*(18), 5627–5634. https://doi.org/10.5194/acp-8-5627-2008

Zahorowski, W., Griffiths, A. D., Chambers, S. D., Williams, A. G., Law, R. M., Crawford, J., & Werczynski, S. (2013). Constraining annual and seasonal radon-222 flux density from the Southern Ocean using radon-222 concentrations in the boundary layer at Cape Grim. *Tellus B*, *65*(1), 19622. https://doi.org/10.13402/tellusb.v19665i19620.19622

Zhang, K., Wan, H., Zhang, M., & Wang, B. (2008). Evaluation of the atmospheric transport in a GCM using radon measurements: Sensitivity to cumulus convection parameterization. *Atmospheric Chemistry and Physics*, *8*(10), 2811–2832. https://doi.org/10.5194/acp-8-2811-2008